

See discussions, stats, and author profiles for this publication at: <https://www.researchgate.net/publication/41806050>

Sliding of Water Droplets on Microstructured Hydrophobic Surfaces

ARTICLE *in* LANGMUIR · MARCH 2010

Impact Factor: 4.46 · DOI: 10.1021/la9044495 · Source: PubMed

CITATIONS

43

READS

59

5 AUTHORS, INCLUDING:



Yang Changwei

Tsinghua University

8 PUBLICATIONS 74 CITATIONS

SEE PROFILE



Pengfei Hao

Beijing Institute of Technology

28 PUBLICATIONS 187 CITATIONS

SEE PROFILE

Sliding of Water Droplets on Microstructured Hydrophobic Surfaces

Cunjing Lv,[†] Changwei Yang,[†] Pengfei Hao,^{*,†} Feng He,[†] and Quanshui Zheng^{*,†,‡}

[†]Department of Engineering Mechanics, Tsinghua University, Beijing 100084, China, and [‡]Department of Mechanical and Aerospace Engineering, Monash University, VIC 3800, Australia

Received November 24, 2009. Revised Manuscript Received February 22, 2010

Sliding behaviors of liquid droplets on solid surfaces are among the fundamental results of wettability. To remedy the lack of quantitative correlation between sliding angle and roughness of the surface, which is known to be effective at enhancing wettability, we report in this paper the observation that the onset of water droplets sliding under gravity on inclined micropillar-structured hydrophobic surfaces always starts with detachment of the rear contact lines of the droplets from the pillar tops. We also establish an explicit analytical model, based on the observed mechanism, by which the sliding angle is fully determined by the fraction of water–solid interface area, droplet volume, and Young’s contact angle. This model gives predictions of sliding angles that agree well with experimental measurements.

Introduction

Superhydrophobicity, typically an effect enhanced by surface roughness on hydrophobic surfaces, has recently attracted great attention because of the easy fabrication of microstructured surfaces^{1–5} with superhydrophobicity and their various applications, such as self-cleaning materials, water collecting means, and friction drag reduction surfaces.^{6–11} Superhydrophobicity is characterized by not only a very large static contact angle ϕ ($> 150^\circ$), but also a very small sliding angle α ($< 5^\circ$).¹² It usually only occurs on hydrophobic surfaces with sufficient roughness.^{1–3,5,12} Its corresponding wetting state is Cassie–Baxter’s¹⁴ in which a water drop attaches to the surface but in a position on top of the rough surface corrugations with air pockets trapped under it. In particular, for the Cassie–Baxter wetting state on a pillar-structured hydrophobic surface as shown, for example, in Figure 1, the static contact angle, ϕ , is correlated with Young’s contact angle,¹³ ϕ_0 , measured on the same

hydrophobic but smooth surface and the fraction of water–solid interface area, f , (defined as the relative area of the pillar tops to the apparent surface area) as follows.¹⁴

$$\cos \phi = -1 + (1 + \cos \phi_0)f \quad (1)$$

Compared with the quantitative knowledge of the static contact angle, little is known about either the mechanisms of liquids sliding on rough surfaces or quantitative relations between sliding angle and roughness.^{15–24}

All proposed relations for sliding angle α of a droplet on a smooth surface can be reduced into the following unified form:^{17,24}

$$\rho g V \sin \alpha = 2Rk \quad (2)$$

where ρ and V denote the droplet mass density and volume, respectively, g the gravity acceleration, R the radius of the wetted area, and k is a constant. Frenkel¹⁵ was probably the first to give a more precise form of the above relation as

$$\rho g V \sin \alpha = 2R\gamma_{LV}(1 + \cos \phi_0) \quad (3)$$

where γ_{LV} is the liquid–vapor interfacial energy and ϕ_0 the Young’s contact angle. Olsen et al.¹⁶ showed good agreement

*Corresponding authors. Prof. Q. S. Zheng: e-mail: zhengqs@tsinghua.edu.cn; Prof. P. F. Hao: e-mail: haopf@mails.tsinghua.edu.cn.

(1) Blosssey, R. Self cleaning surfaces virtual realities, *Nat. Mater.*, **2003**, *2*, 301–306.

(2) Sanchez, C.; Arribart, H.; Guille, M. M. G. Biomimeticism and bioinspiration as tools for the design of innovative materials and systems, *Nat. Mater.*, **2005**, *4*, 277–288.

(3) Ma, M.; Hill, R. M. Superhydrophobic surfaces, *Curr. Opin. Colloid Interface Sci.*, **2006**, *11*, 193–202.

(4) Tuteja, A. et al. Designing superhydrophobic surfaces, *Science*, **2007**, *318*, 1618–1622.

(5) Roach, P.; Shirtcliffe, N. J.; Newton, M. I. Progress in superhydrophobic surface development, *Soft Matter*, **2008**, *4*, 224–240.

(6) Parker, R. P.; Lawrence, C. R. Water capture by a desert beetle, *Nature*, **2001**, *414*, 33.

(7) Lafuma, A.; Quere, D. Superhydrophobic states, *Nat. Mater.*, **2003**, *2*, 457–460.

(8) Lahann, J., et al. A reversibly switching surface, *Science*, **2003**, *299*, 371–374.

(9) Lobaton, E. J.; Salamon, T. R. Computation of constant mean curvature surfaces: Application to the gas–liquid interface of a pressurized fluid on a superhydrophobic surface, *J. Colloid Interface Sci.*, **2007**, *314*, 184–198.

(10) Voronov, R. S.; Papavassiliou, D. V. Review of fluid slip over superhydrophobic surfaces and its dependence on the contact angle, *Ind. Eng. Chem. Res.*, **2008**, *47*, 2455–2477.

(11) Bush, J. W. M.; Hu, D. L.; Prakash, M. The integument of water-walking arthropods: Form and function, *Adv. Insect Physiol.*, **2008**, *34*, 117–192.

(12) Barthlott, W.; Neinhuis, C. Purity of the sacred lotus, or escape from contamination in biological surfaces, *Planta*, **1997**, *202*, 1–8.

(13) Young, T. *Philos. Trans. R. Soc. London*, **1805**, *95*, 65–87.

(14) Cassie, A. B. D.; Baxter, S. *Trans. Faraday Soc.*, **1944**, *40*, 546–551. Lafuma, A.; Quere, D. *Nat. Mater.*, **2003**, *2*, 457–460.

(15) Frenkel, Y. I. J. On the behavior of liquid drops on a solid surface: I. The sliding of drops on an inclined surface, *Exp. Theoret. Phys. (USSR)*, **1948**, *18*, 659.

(16) Olsen, D. A.; Jounier, P. A.; Olson, M. D. The sliding of liquid drops on solid surfaces, *J. Phys. Chem.*, **1962**, *66*, 883–886.

(17) Furmidge, C. G. L. *J. Colloid Sci.*, **1962**, *17*, 309.

(18) Miwa, M.; Nakajima, A.; Fujishima, A.; Hashimoto K.; Watanabe T. Effects of the surface roughness on sliding angles of water droplets on superhydrophobic surfaces, *Langmuir*, **2000**, *16*, 5754–5760.

(19) Roura, P.; Fort, J. Comment on “Effects of the surface roughness on sliding angles of water droplets on superhydrophobic surfaces”, *Langmuir*, **2002**, *18*, 566–569.

(20) Yoshimitsu, Z.; Nakajima, A.; Watanabe, T.; Hashimoto, K. Effects of surface on the hydrophobicity and sliding behavior of water droplets, *Langmuir*, **2002**, *18*, 5818–5822.

(21) Thiele, U.; Knobloch, E. Driven drops on heterogeneous substrates: Onset of sliding motion, *Phys. Rev. Lett.*, **2006**, *97*, 204501.

(22) Dorrier, C.; Rühe, J. Advancing and receding motion of droplets on ultrahydrophobic post surfaces, *Langmuir*, **2006**, *22*, 7652–7657.

(23) Gao, L.; McCarthy, T. J. *Langmuir*, **2006**, *22*, 2966–2967. Gao, L.; McCarthy, T. J. *Langmuir*, **2006**, *22*, 6234–6237.

(24) Wolfram, E.; Faust, R. *Wetting, Spreading, and Adhesion*; Padday, J. F., Ed.; London: Academic Press, 1978; Chapter 10.

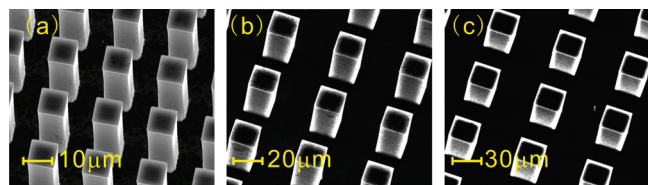


Figure 1. Typical scanning electron microscope (SEM) images of the pillar-structured surfaces with a fixed pillar height ($H = 35 \mu\text{m}$) but different pillar side-lengths and pillar spacings: (a) $a = 10 \mu\text{m}$, $b = 10 \mu\text{m}$; (b) $a = 20 \mu\text{m}$, $b = 30 \mu\text{m}$; (c) $a = 30 \mu\text{m}$, $b = 45 \mu\text{m}$.

between this relation and their experimental observations. Frenkel¹⁵ also associated k with the advancing and receding angles (see Figure 3a for definitions of ϕ_a and ϕ_r) in the form $k = \gamma_{LV}(\cos\phi_r - \cos\phi_a)$, which leads to

$$\rho g V \sin \alpha = 2R\gamma_{LV}(\cos \phi_r - \cos \phi_a) \quad (4)$$

This was experimentally verified by Furmidge.¹⁷

Miwa et al.¹⁸ assumed that relation 2 would also be valid for rough surfaces. They took the same k as for smooth surfaces but corrected the wetted radius R for rough surfaces. For a smooth, flat surface, they give

$$k = \left\{ \frac{9V^2(2 - 3\cos \phi_0 + \cos^3 \phi_0)}{\pi^2} \right\}^{1/3} \frac{\rho g \sin \alpha_0}{6 \sin \phi_0} \quad (5)$$

where α_0 is the sliding angle for smooth surfaces. Substituting eq 5 into eq 2 gives Miwa's model.¹⁸ This model and its validity, however, was later criticized as being conceptually unclear and doubtful.¹⁹ To the best of our knowledge, there are no other analytical models to predict the sliding angle of droplets on rough surfaces.

In the present study, based on experiments exploring the mechanism of sliding on pillar-structured hydrophobic surfaces, we establish an analytical expression of sliding angle α as a function of area fraction f , droplet volume V , and Young's contact angle ϕ_0 —this appears to be the first relationship of this type published.

Sliding Mechanism—Experimental Observation

Sample Preparation. Pillar-structured hydrophobic surfaces were fabricated by photolithography and etching of inductively coupled plasma (ICP), with different side lengths of the square pillars $a = 10, 20$, and $30 \mu\text{m}$, as shown in Figure 1 for three typical samples. The pillars are uniformly distributed in a rectangular grid with six different values, 0.04, 0.0625, 0.1111, 0.16, 0.25, and 0.4444, of the area fraction, where $f = a^2/(a+b)^2$ and b is the spacing between the pillars. In the sample preparation, a $350 \mu\text{m}$ thick (100) silicon wafer was first covered with a photoresist layer by spin coating. Photolithography was then used to transfer the required pattern from a mask to the photoresist layer. The area that was not protected by the photoresist layer was etched by the ICP dry-etching method to finally create the roughness pattern on the wafer. A fixed pillar height ($H = 35 \mu\text{m}$) for all the pillar-structured surfaces studied was achieved by controlling the etching time. After the etching process, the remaining protective layers were removed from the silicon wafer. To make the silicon wafer hydrophobic, a self-assembled monolayer (SAM) of octadecyltrichlorosilane (OTS) of formula $\text{C}_{18}\text{H}_{37}\text{Cl}_3\text{Si}$ (Acros Organics) was used for this purpose. The surface was first treated with a solution of “piranha”, composed of 70% sulfuric acid

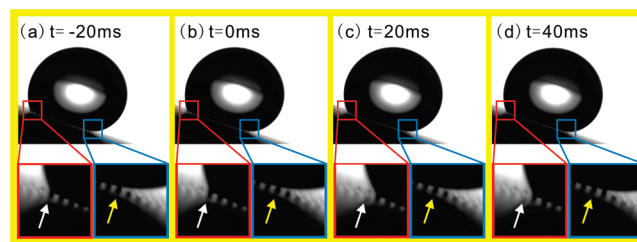


Figure 2. Observation of sliding onset of a $10 \mu\text{L}$ water droplet on a micropillar-structured surface with $a = 30 \mu\text{m}$ and $b = 45 \mu\text{m}$. The enlarged pictures of (a) and (b) show the state in the last moment before onset of sliding. Those of (c) shows that sliding starts as the rear contact line detaching from the top of a pillar and jumping to the next pillar; meanwhile, the front line is remaining adhered to the same pillar. Those of (d) show that a cycle of sliding is completed with the front contact line jumping to the next pillar. See also two movies in the Supporting Information.

(H_2SO_4) solution with 98% concentration and 30% hydrogen peroxide (H_2O_2) solution with 20% concentration. The process consists of immersing the surface in the solution of “piranha” and keeping it at a constant temperature of 90°C for 30 min inside a heater. The surface was then rinsed with deionized water and dried. In a completely dry container, 0.1 mL of OTS is mixed with 25 mL of hexadecane. The surface was rinsed with this new solution and baked in an oven for 20 min. Then, the surface was treated with chloroform for 15 min to remove any dust, and finally, the surface was soaked in anhydrous alcohol for 30 min and dried. After chemical modification, the Young's contact angle ϕ_0 was measured to be 105° on the smooth surface.

Sliding Mechanism. The static contact angles (ϕ) and sliding angles (α) were measured with a commercial contact angle meter (JC2000CD1). In our experiments, water droplets with volumes of 5, 10, and $15 \mu\text{L}$ were quasi-statically placed on the samples by a microsyringe automatically, and images of the droplets on the samples recorded instantaneously using a digital camera. Sequential photographs of the water droplets were taken every 10 ms with the computer-controlled digital camera. As we increased the slope of the sample from the horizontal state, the droplet on it initially became increasingly inclined downward. At a critical slope angle, the sliding angle, α , was reached, and we observed two types of motions depending on how quickly the slope was increased. In a normal experiment, the slope was increased continuously by being driven by a motor at 1.5° per second. In this case, we observed that the droplet would start a continuously sliding motion immediately after the sliding angle was reached (see Movie 1, Supporting Information). No details of the detachment and/or attachment at the onset of sliding could be observed. On the other hand, as the slope of the sample was increased sufficiently slowly as it approached α , we found that the rear contact line of the droplet would detach from the edge of the pillar and then quickly jump to the next pillar. During this process, the front contact line remained adhering and did not move (see Movie 2, Supporting Information). With a further slight increase of the slope, the droplet began to move downward.

More details of the sliding onset as the slope was increased very slowly are described below. Figure 2 shows four continuous images (with time interval of 20 ms) of a $10 \mu\text{L}$ droplet on a pillar-structured surface ($a = 30 \mu\text{m}$ and $b = 45 \mu\text{m}$), with respective enlarged pictures of the front and rear contact lines. The images shown in Figure 2a,b were captured at 20 ms interval just before the sliding onset. The white and yellow arrows in the enlarged images of Figure 2a,b indicate that the pillars adhered by the rear and front contact lines of the water droplet. These same

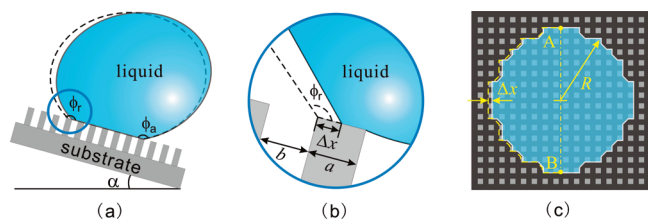


Figure 3. Schematic illustration of the sliding onset of a water droplet on a micropillar-structured surface: (a) side view of the droplet–surface system, where the dashed and solid lines represent the positions of the meniscus before and just after the onset of sliding; (b) enlarged view of the rear contact line on the top of the micropillar, where Δx represents the virtual displacement of the rear contact line; (c) top view of the three-phase contact line on the surface.

pillars are indicated in all the enlarged images in Figure 2a–d. The observation that these pillars are the same in Figure 2a,b implies that the droplet in both states of Figure 2a,b is at a stage prior to the sliding. Figure 2c shows the picture and its enlarged images of the droplet at 20 ms after Figure 2b. The pillar adhered to by the rear contact line in Figure 2c is the one next to the pillar indicated by the white arrow, while the pillar adhered to by the front contact line in Figure 2c is the same one as in Figure 2a,b, i.e., the pillar indicated by the yellow arrow. These observations reveal that the sliding onset happened at a moment between $t = 0$ (Figure 2b) and $t = 20$ ms (Figure 2c), and that the sliding onset is initiated by the detachment of the rear contact line, in spite of the front contact line remaining adhered. The jump of the rear contact line from one pillar to the next within 20 ms reveals also that the detachment speed from the pillar top ($30\ \mu\text{m}$ in width) is quicker than $1.5\ \text{mm/s}$. Figure 2d shows the images at 20 ms after Figure 2c. By examining the adhered pillars at the rear and front contact lines in Figure 2d and comparing those with the ones indicated by the white and yellow arrows, one can see that while the rear contact line remains adhered to the surface the front contact line made a jump (to the next pillar). Successive sliding motion would arise from a continuous sequence of the above-described detachment–attachment process. Here, we emphasize that such motion features were observed in all our experiments of water droplets sliding on the pillar-structured surfaces for which $a \geq 20\ \mu\text{m}$. Due to the resolution limit of the camera used, the configurations of the smaller micropillars could not be observed clearly. We believe, however, that the mechanism causing the onset and progression of the sliding motion on pillar-structured surfaces with finer pillars, or even non-square-shaped pillars, would be the same. This sliding mechanism is, to the best of our knowledge, revealed and reported here for the first time.

The movement of a droplet on a surface is associated with a movement of the three-phase contact line. This movement would be continuous on an ideally smooth surface, but may be discontinuous on a rough surface, as we have observed, with the rear contact line of the droplet jumping from the rearmost pillar to its next and then the front contact line proceeding from the foremost pillar to its next. In fact, our experimental observation has justified some of the speculations proposed by other authors about wetting behaviors for which the motion of the contact line is critical.^{15,17,22,23} Frenkel¹⁵ believed that the only mechanism for a drop to run down is “pouring” of the fluid from the rear edge to the front edge of the drop, similar to that for motion of a caterpillar tractor, and that such “pouring” begins only when the work of the gravitational force is greater than or equal to the work of adhering forces of the droplet’s rear edge. Under the hypothesis that the liquid meniscus successively jumps from one post at a time, Dorrer and R  he²² proposed that the energy

barrier to be overcome by a meniscus detaching from a row of posts is mainly a function of the contact area between the drop and an individual post and concluded that the advancing contact angle will reach 180° during the advancing motion. Gao and McCarthy²³ also emphasized that the activation energy for receding is greater than that for advancing of a drop on a microstructured surface. These propositions or analyses are qualitatively correct but are insufficient for establishing a quantitative correlation of the sliding behavior with roughness. Our experimental results clearly show that the receding contact line governs the movement of the droplets on the micropillar-like surfaces. An additional discovery in all our experiments is that the micropillars appear either fully inside or fully outside the wetting area (see Figure 2), conforming to the local energy minimum principle. In other words, once the rear contact line detaches itself from the outer boundary of a micropillar (see Figure 2b,c), it would move rapidly and attach to the outer boundary of the next pillar until initiation of the next cycle; once the advancing contact angle becoming large enough, the advancing contact line will proceed abruptly to the outer boundary of the next pillar and stay there until next cycle; no contact line would ever stop in the middle of a single micropillar. This experimental observation may challenge some previous assumptions (e.g., that the rear contact line might rest at a section of the pillar top edge even though the water has been detached from the whole pillar top surface, as implied in Figure 7 in ref 22.).

Sliding Angle Model and Experimental Verification

Theoretical Model. The above experimental observation reveals that the sliding angles of water droplets on micropillar-structured surfaces are determined by the onset of detaching movement of the rear contact line (Figure 2). To model such a process, we consider a virtual detaching movement of the receding contact line of the water droplet (Figure 3) with the advancing contact line resting on its initial position on the surface. To devise a simple model without loss of the physical essence, we assume that the virtual distance linearly decreases from its maximum, Δx ($\Delta x \ll a$), at the rearmost point to zero at both division points A and B between the advancing and receding contact lines (Figure 3c). So, modeled detaching movement corresponds to a differential area $\Delta S = \Delta x R a / (a + b)$, which is added to the solid–vapor interface plus the liquid–vapor interface while at the same time being subtracted from the solid–liquid interface, leading to a change of the total interfacial energy equal to

$$\Delta E = (\gamma_{\text{SV}} + \gamma_{\text{LV}} - \gamma_{\text{SL}}) \Delta S = \gamma_{\text{LV}} (1 + \cos \phi_0) \Delta x R \sqrt{f} \quad (6)$$

in which the Young’s relation²² $\gamma_{\text{LV}} \cos \phi_0 = \gamma_{\text{SV}} - \gamma_{\text{SL}}$ and the definition $f = a^2 / (a + b)^2$ have been used.

Such a virtual detachment must result in a virtual downward inclination of the droplet (Figure 3a). For simplicity, the downward distance of the gravity center of the droplet along the surface is approximated as $\Delta x/2$. The corresponding decrease in gravity potential is consequently equal to $(\Delta x/2) \rho g V \sin \alpha$. The condition for sliding onset, therefore, can be expressed in terms of the total energy balance, which leads to, with the kinetic energy and heat dissipation ignored, the relation

$$\rho g V \sin \alpha = 2 R \gamma_{\text{LV}} (1 + \cos \phi_0) \sqrt{f} \quad (7)$$

This reflects the effect of roughness on sliding angle through not only the apparent wetted radius R , but also the square root of the area fraction $f^{1/2}$. This relation is novel for the rational theoretical analysis based on an experimentally uncovered mechanism.

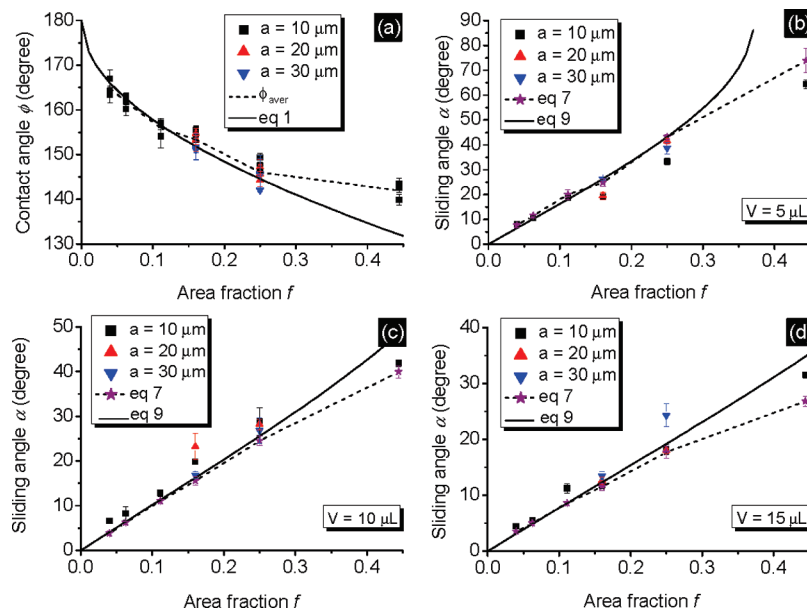


Figure 4. Static contact angles (a) and sliding angles (b–d) vs area fractions. The dots with error bars are the measured values and the solid lines are the predictions by Cassie–Baxter model (eq 1) and by the sliding angle model (eq 9). The average values of the measured contact angle ϕ_{aver} are linked by a dashed polyline in (a), which is combined with the sliding angle model (eq 7) to give predictions of the sliding angle as shown by the dashed polylines in (b–d).

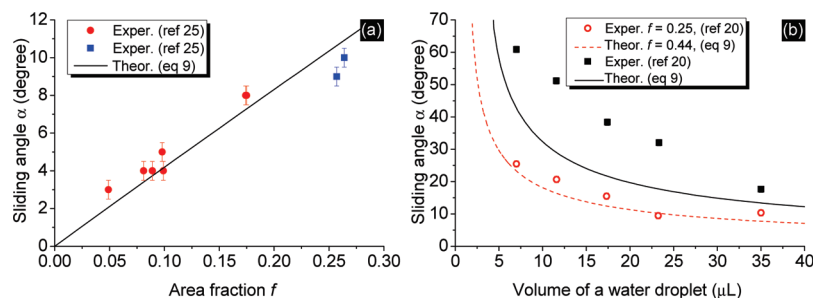


Figure 5. Comparison of eq 9 with other references: (a) data from ref 25. ($\phi_0 = 120.6^\circ$, $V = 15 \mu\text{L}$); (b) data from ref 20. ($\phi_0 = 114^\circ$).

We can further express the radius R of the apparent wetted area in terms of the droplet volume V and the static contact angle ϕ in the following form:

$$R = \left[\frac{3V}{\pi(2 - 3\cos\phi + \cos^3\phi)} \right]^{1/3} \sin\phi \quad (8)$$

Combining eqs 1, 7, and 8 yields the following equation:

$$\sin\alpha = \frac{2\sqrt{3}\gamma_{LV}}{\rho g \sqrt{\pi V^2}} \frac{\sqrt{2(1 + \cos\phi_0) - (1 + \cos\phi_0)^2 f}}{\sqrt{4 - 3(1 + \cos\phi_0)^2 f^2 + (1 + \cos\phi_0)^3 f^3}} (1 + \cos\phi_0) f \quad (9)$$

This sliding angle model determines sliding angle α fully in terms of such known physical properties as area fraction f , droplet volume V , and Young's contact angle ϕ_0 , instead of relying on an unknown coefficient like k in eq 2, or the uncertain advancing and receding angles as in eq 4.

Experimental Verification. The dots with the error bars in Figure 4a show the measured static contact angles, and those in Figure 4b–d plot the sliding angles for droplets of volumes $V = 5$, 10, and 15 μL vs the area fractions f , respectively. The solid lines in those figures are the contact angle ϕ predicted by the

Cassie–Baxter model eq 1 and the sliding angle α predicted by the sliding angle model eq 9. The average values of measured static contact angles for droplets with different volumes (ϕ_{aver}) are linked by the dashed polyline in Figure 4a as the function of area fractions f . The dashed polylines in Figure 4b–d are the predictions by the sliding angle model eq 7 with R determined by eq 8 from droplet volume V and the measured static contact angle ϕ rather than that predicted by eq 1.

The comparisons in Figure 4 show excellent agreement of the sliding angle model (eq 9) with our measured values for all area fractions lower than 0.25. Notable deviations, however, appear for the larger value of f ($= 0.4444$). To further check the validity of our model, we have found two articles^{20,25} that gave systematical measurements of sliding angles on microscale pillar-structured surfaces with flat pillar tops. Figure 5 shows the comparisons between their measurements (dots) and our theoretical predictions (lines). It is seen again that, for all comparably lower area fractions ($f \leq 0.26$), the model predictions agree very well with the measured, and notable deviation appear at $f = 0.44$. Why the comparably larger deviations appear for a large f is an open issue to be investigated in the future.

(25) Fürstner, R.; Barthlott, W. Wetting and self-cleaning properties of artificial superhydrophobic surfaces, *Langmuir* **2005**, *21*, 956–961.

Interestingly, although the model eq 9 is developed based on the observed sliding onset and process mechanisms for square-shaped pillar-structured surfaces, we find it may be still applicable for some non-square-shaped pillars. The red circular and blue square dots in Figure 5a are plotted from the measured sliding angles in another lab (ref 25). The corresponding pillar cross sections are circular and square. We see that these measured results agree very well with the model prediction from eq 9, using the same static contact angle ($\phi_0 = 120.6^\circ$) and water droplet volume ($V = 15 \mu\text{L}$) as those given in ref 25. We need, however, to check the general validity or nonvalidity of eq 9 for various pillar cross sections in future research.

Concluding Remarks

In this paper, we report an observation of the sliding onset mechanism of water droplets on rough surfaces—sliding of water droplets on pillar-structured surfaces, with the pillar sizes ranging from 10 to 30 μm , always starts from the detaching of their rear contact lines with the front contact lines remaining adhesive. On the basis of this observation, we establish an explicit analytical model that determines the sliding angles completely in terms of the physical properties: area fraction f , the droplet volumes V , and the Young's contact angle ϕ_0 . We also verify the model predictions of sliding angles with experiments. This has been done for a number of pillar-structured surfaces with different area fractions as well as pillar sizes. To the best of the authors' knowledge, this model is the first to quantitatively correlate sliding angles directly with the roughness of the surface.

Although the model eq 9 was established for pillar-structured surfaces with square-distributed square cross-sectional

pillars, we believe that a slight modification in the following form

$$\sin \alpha = \frac{k\gamma_{LV}}{\rho g \sqrt[3]{\pi V^2}} \frac{\sqrt{2(1 + \cos \phi_0) - (1 + \cos \phi_0)^2 f}}{\sqrt[3]{4 - 3(1 + \cos \phi_0)^2 f^2 + (1 + \cos \phi_0)^3 f^3}} (1 + \cos \phi_0) f \quad (10)$$

would be applicable for all pillar-structured surfaces with flat tops, where the coefficient k reflects the combined effect of pillar cross-section and pillar distribution. Further theoretical and experimental works for verifying eq 10 are under way. It is unclear if eq 10 would be applicable or not for other types of roughness (such as re-entrant surfaces, fractal structures, and dual-scale roughness), and for pillars with submicrometer or even nanoscale sizes.

Acknowledgment. Financial support from the NSFC through grants no. 10672089 and no. 10772100 is gratefully acknowledged.

Note Added after ASAP Publication. This article was published ASAP on March 5, 2010. Figure 5b has been modified. The correct version was published on March 10, 2010.

Supporting Information Available: Observation of motion of a 10 μL water droplet on a micropillar-structured surface with $a = 30 \mu\text{m}$ and $b = 45 \mu\text{m}$. The true time was 0.65s for SI_Movie_1 and 3.3s for SI_Movie_2, respectively. This material is available free of charge via the Internet at <http://pubs.acs.org>.